

Modeling and Characterization of a Voice Coil Motor

by

Ashley Brown

Submitted to the  
Department of Mechanical Engineering  
in Partial Fulfillment of the Requirements for the Degree of

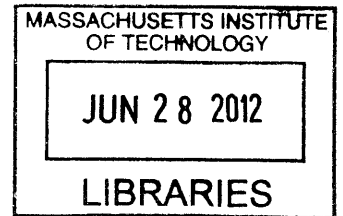
Bachelor of Science in Mechanical Engineering

at the

Massachusetts Institute of Technology

June 2012

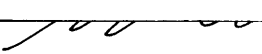
**ARCHIVES**

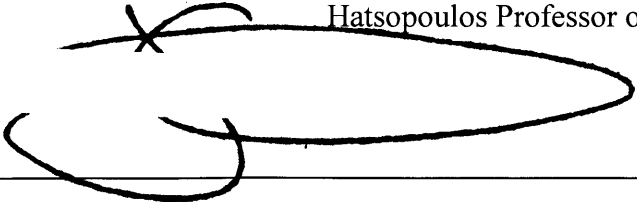


© 2012 Ashley Brown. All rights reserved.

The author hereby grants to MIT permission to reproduce and to distribute publicly paper and electronic copies of this thesis document in whole or in part in any medium now known or hereafter created.

Signature of Author: \_\_\_\_\_  
 Department of Mechanical Engineering  
May 21, 2012

Certified by: \_\_\_\_\_  
 Ian W. Hunter  
Hatsopoulos Professor of Mechanical Engineering  
Thesis Supervisor

Accepted by: \_\_\_\_\_  
 John H. Lienhard V  
Samuel C. Collins Professor of Mechanical Engineering  
Undergraduate Officer



# Modeling and Characterization of a Voice Coil Motor

by

Ashley Brown

Submitted to the Department of Mechanical Engineering  
on May 21, 2012, in partial fulfillment of the  
requirements for the degree of  
Bachelor of Science in Mechanical Engineering

## Abstract

This thesis describes the development of a voice-coil motor that will allow viscous fluids to be delivered via a portable needle-free injection device. The chosen motor design features opposing magnets whose flux is channeled across the air gap by a center radial magnet, thus creating a higher flux density in the gap compared to a one-magnet design. An analytical model is developed which gives the force of the motor based on the material properties and geometry. An optimized geometry is modeled using finite element analysis, which predicts a motor constant of  $11.02 \text{ N}/\sqrt{\text{W}}$ . The motor is fabricated and characterization reveals it to have a motor constant of  $8.43 \text{ N}/\sqrt{\text{W}}$ . Although the motor constant is less than expected, it is a large improvement over the current motor used in needle-free injection, which has a motor constant of  $3.21 \text{ N}/\sqrt{\text{W}}$ .

Thesis Supervisor: Ian W. Hunter

Title: Hatsopoulos Professor of Mechanical Engineering



## Acknowledgments

I would like to thank Bryan Ruddy for his continual willingness to share his amazingly broad knowledge. Thank you for patiently guiding me through this process, and for taking the time to teach me everything from diverse machining techniques to detailed electromagnetic theory. I am a much better engineer because of it.

Thank you also Professor Ian Hunter for inviting me to work in your lab, and for your support for my research. I have treasured the opportunity to work here, both because I have learned so much, and because of the genial and impressive people in the lab.

Thank you Alison Cloutier for your willingness to help me with any problem, no matter how small. Thank you Mark Belanger for allowing me to work in your machine shop, and for the good machining advice you generously gave. Thank you Cathy Hogan for teaching me about the applications for the motor. Thank you David Rolnick for your assistance in finishing this work.



# Contents

<b>Contents</b>	<b>7</b>
<b>1 Introduction</b>	<b>9</b>
<b>2 Background</b>	<b>11</b>
2.1 Voice Coil Motors . . . . .	11
2.1.1 Lorentz Force . . . . .	11
2.1.2 Magnetic Circuit . . . . .	12
2.1.3 Motor Constant . . . . .	13
2.2 Needle Free Injection . . . . .	14
2.2.1 Jet Injector Background . . . . .	14
2.2.2 NFI Voice Coil Development . . . . .	15
<b>3 Theory and Modeling</b>	<b>17</b>
3.1 Motor Geometry . . . . .	17
3.2 Field Solutions . . . . .	19
3.2.1 Poisson's and Laplace's Equations . . . . .	19
3.2.2 Boundary Conditions . . . . .	21
3.2.3 Field Solutions for this Geometry . . . . .	21
3.3 Geometric Optimization . . . . .	24
3.4 Finite Element Modeling . . . . .	25

<b>4</b>	<b>Experiment</b>	<b>29</b>
4.1	Mechanical Design and Manufacturing . . . . .	29
4.1.1	Endcaps . . . . .	31
4.1.2	Housing . . . . .	31
4.1.3	Bobbin . . . . .	32
4.1.4	Coil . . . . .	34
4.1.5	Magnets . . . . .	35
4.1.6	Alignment Tool . . . . .	36
4.2	Testing and Characterization . . . . .	36
4.2.1	Experimental Setup . . . . .	37
4.2.2	Experimental Results . . . . .	38
<b>5</b>	<b>Conclusion</b>	<b>43</b>
	<b>Bibliography</b>	<b>45</b>



# Chapter 1

## Introduction

Needle Free Injection (NFI) is a promising technology that has several advantages over conventional injection. While maintaining equivalent effectiveness [1], NFI eliminates the use and disposal difficulties associated with hypodermic needles. In addition, NFI is well suited for mass injections or injections to animals [1].

In NFI, a fluid at high pressure is forced through a small orifice, forming a jet. This jet penetrates the skin and delivers the drug to the tissue. The Bioinstrumentation Laboratory at MIT has developed a NFI device powered by a voice coil motor which is shown in Fig. 1-1.

The device shown has the ability to dictate the pressure of the liquid throughout the stroke. This shaped waveform gives control over the injection depth and volume, and potentially reduces the risk of contamination [2]. One application being developed with this NFI device is the delivery of monoclonal antibodies directly to the target area. These molecules could be used to treat cancer or autoimmune diseases. In particular, the jet injector could be used to deliver these biotherapeutic drugs directly to the joints of rheumatoid arthritis patients, and in a manner that is much less painful than conventional injections.

Monoclonal antibodies are composed of large molecules that tend to aggregate when placed in high concentrations. Thus, the higher the concentration of a solution,

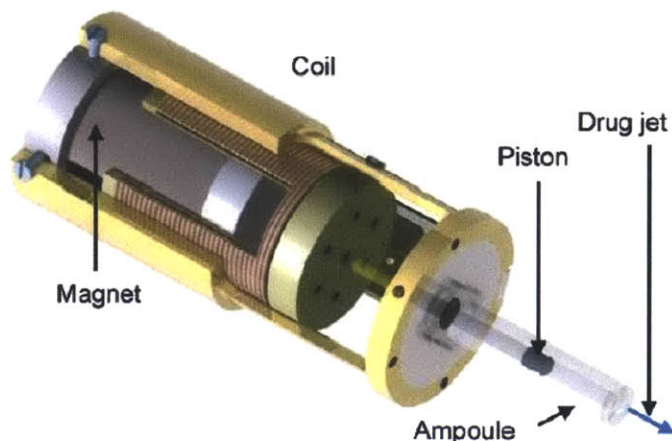


Figure 1-1: A schematic of the current NFI device. The coil of the voice coil motor is attached directly to a piston, which forces the drug through a small orifice and into a jet (reproduced from [2]).

the higher the viscosity [3]. The current jet injector is able to deliver fluids with viscosities of up to 20 mPa·s. With this capability, four injections are needed to deliver a full dose of monoclonal antibodies. A more powerful actuator would allow the jet injector to deliver higher concentrations of monoclonal antibodies, decreasing the number of injections needed and easing the burden on the patient.

Another application under development is the delivery of poly(ortho esters), which are polymers that can be used to deliver drugs into the body and then slowly release the drugs over time. With this slow release method, injections are needed less frequently [4]. This technology, similar to monoclonal antibodies, is limited by the high viscosity of the solution and would benefit from a more powerful NFI device.

This thesis describes the development of a voice coil motor that will provide more force, enough to inject higher concentrations of monoclonal antibodies and poly-orthoesters. This motor remains light enough to be part of a portable device. A model to predict the force of the actuator is developed, and a final design is prototyped and characterized.

# Chapter 2

## Background

The effectiveness of a NFI device depends in large part on the actuator. This chapter introduces the basic operation of voice coil motors and their use in NFI. Force generation, magnetic circuits, and the motor constant are discussed. Then, the history of and requirements for needle free injection are considered.

### 2.1 Voice Coil Motors

#### 2.1.1 Lorentz Force

A voice coil motor is a type of a Linear Lorentz-force Actuator. Commonly used in loudspeakers, the actuator is also used to position the read arm in hard drives and the lens in CD drives. In voice coils, a coil of wire passes through a region of high magnetic field. The coil is mechanically constrained to move linearly, such that when current runs through the coil, the actuator produces a linear force which is governed by the Lorentz Force Law. The force  $F$  produced by the actuator is given by

$$F = BJV, \tag{2.1}$$

where  $B$  is the magnetic flux density (T),  $J$  is the current density flowing perpendicular to the magnetic field ( $A/m^2$ ), and  $V$  is the volume of the conductor exposed to the magnetic field. This equation assumes that the magnetic field is constant across the geometry; in actual motors, an integral is needed to evaluate the force. Yet even when an integral is used, the force of the actuator is still dictated by the strength of the magnetic field, the magnitude of the current density, and the amount of conductor exposed to magnetic field [5].

### 2.1.2 Magnetic Circuit

Permanent magnets are frequently used to generate the magnetic field. In order to maximize the effectiveness of the magnets field, iron or another material of high magnetic permeability is placed to direct the magnetic flux, as is shown in Fig. 2-1. The magnetic flux is guided from one pole of the magnet to the other, thus forming a complete loop and creating what is called a magnetic circuit. At one point in the magnetic circuit, the guiding iron is interrupted by a gap of air. The iron channels the magnetic flux through this small gap, creating a high magnetic field in the region. The wire coil is placed so as to intersect this region of high magnetic field.

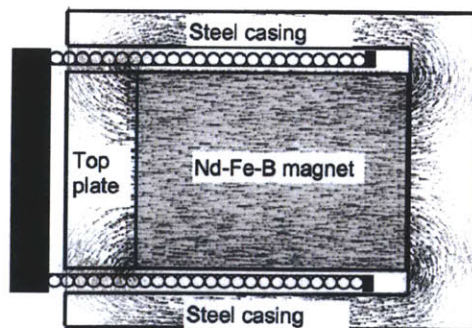


Figure 2-1: A schematic of a magnetic circuit. The black dashes represent magnetic flux lines, which are generated by the magnet. The steel casing and top plate direct the flux from one pole of the magnet to the other, in one point channeling the flux across an air gap where it intersects the coi (reproduced froml [6]).

### 2.1.3 Motor Constant

A common parameter used to evaluate motor performance is the motor constant, which is defined as the force produced divided by the square root of the power consumed. The power consumed is due to ohmic losses in the coil, and is thus given by

$$P = J^2 V / \sigma, \quad (2.2)$$

where  $P$  is the power consumed (W), and  $\sigma$  is the conductivity of the coil (S/m). Thus the force constant is given by

$$\epsilon = \frac{F}{\sqrt{P}} = B \sqrt{\frac{\sigma M}{\rho_c}}, \quad (2.3)$$

where  $M$  is the mass of the conductor (kg), and  $\rho_c$  is the density of the conductor ( $\text{kg}/\text{m}^3$ ). It is noteworthy that the motor constant does not depend on current; for a given motor, the magnetic field and geometric parameters fully define the motor constant. As a means to compare two motors, the motor constant is imperfect, because it is coupled to the mass of the motor. As an illustration of this point, consider a motor that produces a force  $F$  while consuming a power  $P$ . Now imagine that a second, identical motor is placed beside the first, and the two are considered as one unit. Now, the two motors produce a force of  $2F$  while consuming  $2P$ . Using Eq. 2.3, it can be seen that the motor constant of the two motor unit has increased by a factor of  $\sqrt{2}$  compared to the motor constant of a single unit. Thus, the motor constant scales with the square root of the mass, making it difficult to compare motors of different masses. Dividing the motor constant by the square root of the total mass  $\epsilon/\sqrt{M}$  scales the motor constant such that meaningful comparisons can be made between motors of different sizes [5]. With this metric, motors of the same geometric type should have the same value, regardless of size scale. In an actuator meant for a portable NFI device, both the motor constant and the total mass are im-

portant considerations. By calculating the mass-scaled motor constant, it is possible to measure how well a design would perform in these lightweight applications.

## 2.2 Needle Free Injection

### 2.2.1 Jet Injector Background

A jet injector delivers a dose of drug to tissue without the use of needles. To do so, high pressures are applied to the liquid drug, which is forced through a narrow aperture. This high speed jet of liquid penetrates the skin, and the drug is delivered to the underlying tissue [2].

NFI delivers the drug with as much or more effectiveness as a hypodermic needle, while eliminating some of the negative aspects of the needles. First, the risk of healthcare workers being injured by the needles is eliminated. Likewise eliminated is the risk of contamination from spent needles, as well as the costly burden of properly disposing of the needles. Furthermore, some people prefer the sensation of NFI over that of conventional injection, and the technology may be helpful to those with belonephobia, or fear of needles. Lastly, the jet injector provides an ideal platform for mass vaccinations and drug delivery to animals [1].

The first jet injector was invented in the nineteenth century, and systems have been commercially available since the mid-twentieth century. These systems have a common mode of operation: they use a high force, high power actuator to drive a piston which forces the liquid through a narrow nozzle, forming the jet. Actuators on current commercially available models include springs, high pressure gas, explosive chemicals, or piezoelectric actuators. With the exception of the piezoelectric actuator, none of these systems have the possibility of a controllable pressure profile within a single injection [2].

A controlled, varying pressure profile is particularly desirable because it could eliminate a problem that led the World Health Organization and the US military to

discontinue use of Multi-Use Nozzle Jet Injectors. It was found that near the end of the jet injector's stroke, the applied pressure decreased, which would sometimes allow a small quantity of fluid and blood to flow back into the nozzle. This backflow posed a risk of spreading Hepatitis B [6].

A jet injector developed in the MIT Bioinstrumentation Laboratory has the ability to control the pressure profile throughout the injection, potentially reducing this risk. The system employs a Linear Lorentz-force Actuator, a voice coil motor. Because the voice coil is excited with electricity, its force output can be controlled throughout the stroke length. The Bioinstrumentation Laboratory's injector employs closed-loop control over the pressure profile. With this system, the Laboratory has been able to shape waveforms such that the depth and volume of injection can be controlled independently [2].

During injection, the depth of penetration depends on the peak pressure applied. Recent tests performed in the Bioinstrumentation Laboratory have applied pressures ranging from 5 MPa to 50 MPa, and have produced jet velocities ranging from 10 m/s to 100 m/s [1, 2].

### **2.2.2 NFI Voice Coil Development**

Current jet injectors in the Bioinstrumentation Laboratory use a custom-designed voice coil motor [2]. The motor has the same general form that was shown in Fig. 2-1 [6].

The magnet is composed of two NdFeB magnets [7]. The surrounding steel casing, made of 1026 steel, creates a magnetic circuit, channeling the magnetic flux from the magnet across the small air gap, where it reaches the iron top plate and reenters the magnet. The coil sits in the air gap, its current flowing perpendicular to the magnetic field and thus generating the axial force.

The coil consists of 582 turns of 28 gauge (0.320 mm diameter) wire, 6 layers deep. The moving mass is about 50 g, and the total mass is about 500 g. The stroke is 30

mm [2]. A magnetic flux density of 0.6 T was measured in the gap [7]. The actuator has a motor constant of  $3.21 \text{ N}/\sqrt{\text{W}}$ , and thus the value for the motor constant divided by the square root of the total mass is  $4.54 \text{ N}/\sqrt{\text{W} \cdot \text{kg}}$ . The actuator is able to produce a maximum force of  $\pm 200 \text{ N}$ .

As Nate Ball notes in his thesis [6], there is limited room for improvement in this design. The force generated depends only on the strength of the magnetic field and on the volume and current density of the coil. Improvements can come from advanced materials and optimized geometries, but the impact of these changes on this one-magnet design is limited.



# Chapter 3

## Theory and Modeling

This section presents the laws and methods used to design the motor. The chosen geometry is described, and the magnetic fields for this geometry are found using Poisson's and Laplace's equations. The optimization of the design is described, as is the validation using finite element analysis.

### 3.1 Motor Geometry

It is desired to build a motor that has a significantly higher motor constant than the motor currently used in jet injectors. Thus, the chosen design is more than an incremental improvement of materials or minor adjustment of geometry. The design gains most of its improvement by shaping the magnetic flux to create a region of stronger magnetic field. To do so, the design has two axially-oriented permanent magnets, both of which point towards the center of the motor. At the motor's center, the fields from the two magnets collide and are forced outwards into the air gap. Fed by these two magnets, the field in the gap is double the strength of the one-magnet design.

Between the two opposing axial magnets is a radial magnet, whose purpose is to help direct the magnetic flux from the axial magnets into the air gap. The  $\mathbf{B}$  field

must form a complete loop, and the radial magnet helps it do so by attracting the field and channeling it outwards, where it can follow the iron shell and complete the magnetic circuit. A diagram of the design is given in Fig. 3-1.

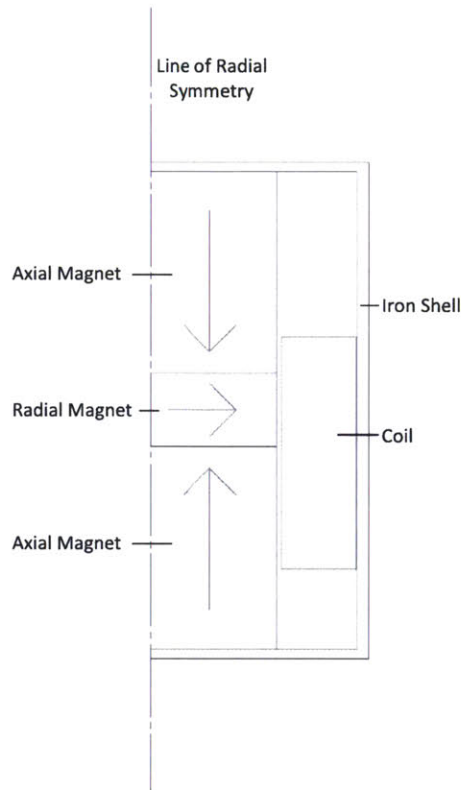


Figure 3-1: A schematic of the motor design. The dashed line on the left represents an axis of radial symmetry. The outermost region is the iron shell. Within the shell on the left are the opposing axial magnets separated by a radial magnet. To their right is an air gap with the coil inside.

Existing designs use iron in place of the radial magnet. The disadvantage of using iron is that iron is susceptible to saturation. In some parts of its travel, the magnetic flux generated by the coil will reinforce the flux from the magnets. If this increase in flux is high enough, then the iron will saturate, meaning that the iron is no longer able to direct all the flux through the coil and across the air gap. Thus, when the iron saturates, there is a smaller gain in force for a given increase in current, that is, the motor constant decreases. If the iron is replaced by a radial magnet, however,

then there is no danger of saturation, and the motor constant will not change for this reason at high levels of current. The chosen design, therefore, is particularly suited for high current, high force applications.

## 3.2 Field Solutions

### 3.2.1 Poisson's and Laplace's Equations

In order to calculate the expected force from the motor, the magnetic fields in the air gap must be known. The fields in the magnets and the air gap can be found by solving the governing equation. Within the magnets, the fields must satisfy Poisson's equation, which can be derived from Maxwell's equations.

Magnetic Gauss's Law states that

$$\nabla \cdot \mathbf{B} = 0, \tag{3.1}$$

where  $\mathbf{B}$  is the magnetic flux density (T). Therefore, there exists a vector  $\mathbf{A}$  such that

$$\mathbf{B} = \nabla \times \mathbf{A}. \tag{3.2}$$

This vector  $\mathbf{A}$  is called the magnetic vector potential. The divergence of  $\mathbf{A}$  may be defined as equal to any constant; it is convenient to set this constant equal to zero. Using this condition, it is possible to say that

$$\nabla \times \mathbf{B} = \nabla \times \nabla \times \mathbf{A} = \nabla(\nabla \cdot \mathbf{A}) - \nabla^2 \mathbf{A} = -\nabla^2 \mathbf{A}. \tag{3.3}$$

By making use of Ampere's Law and the relation between magnetic fields and magnetic flux density, it is possible to derive Poisson's equation for permanent magnets. Ampere's law is given by

$$\nabla \times \mathbf{H} = \mathbf{J} + \frac{\partial \mathbf{D}}{\partial t}, \quad (3.4)$$

where  $\mathbf{H}$  is the magnetic field (A/m),  $\mathbf{J}$  is the current density in the region (A/m<sup>2</sup>), and  $\mathbf{D}$  is the electric displacement field (C/m<sup>2</sup>). In the regions of interest, both the current density and the time rate of change of the electric displacement field are equal to zero. Magnetic flux density is related to magnetic field by

$$\mathbf{B} = \mu(\mathbf{H} + \mathbf{M}), \quad (3.5)$$

where  $\mu$  is the permeability of the material (H/m), and  $\mathbf{M}$  is the magnetization of the material (A/m). Thus, using Eqs. 3.4 and 3.5, Poisson's equation within permanent magnets is given by

$$\nabla^2 \mathbf{A}_{\text{magnet}} = -\mu \nabla \times \mathbf{M}. \quad (3.6)$$

In the air gap, the fields must satisfy Laplace's equation, which is derived using the same conditions and is given by

$$\nabla^2 \mathbf{A}_{\text{air}} = \mathbf{0}. \quad (3.7)$$

There exist a finite number of solutions to Poisson's and Laplace's equations for a given type of geometry. The actual solution of a particular geometry is a superposition of one or more of the possible solutions of the equation. Complete solutions of the equations are the products of functions that vary in only one of the three possible coordinates. So, for example, if a particular geometry had field variations in  $x$  and  $y$  but not in  $z$ , the solution to Poisson's or Laplace's equation would be the product of a function that depended only on  $x$  and a function that depended only on  $y$ . A voice coil motor can be described in cylindrical coordinates, with the field varying in  $r$  and  $z$  but not in  $\theta$ . For this geometry, the solution to Poisson's Equation (3.6) in

the radial direction is given by Struve functions, and the radial solution to Laplace's Equation (3.7) by Bessel functions. In Laplace's equation, the solution in the axial direction is given by exponential functions [5].

### 3.2.2 Boundary Conditions

In addition to satisfying Poisson's and Laplace's equations, the field solutions must also satisfy boundary conditions. There are two important boundary conditions for voice coils. First, assuming that no surface currents are present, then the component of the  $\mathbf{H}$  field that is parallel to a boundary must be continuous across the boundary. Second, the component of the  $\mathbf{B}$  field that is perpendicular to a boundary must be continuous across that boundary.

### 3.2.3 Field Solutions for this Geometry

To solve for the field within the coil and the air gap, the magnetization of the permanent magnets must be made numerically tractable. The magnetization is a constant value within each magnet, an axial magnetization in the axial magnet, and a radial magnetization in the radial magnet. To solve the field equations, it is convenient to represent the magnetization as a Fourier series, and the field can be solved for each harmonic separately. The total field can then be found by summing all the harmonics. A Fourier series describing the magnetization is given by

$$\mathbf{M} = \sum_{n \text{ odd}} [M_{rn} \cos(nkz)\hat{\mathbf{r}} + M_{zn} \sin(nkz)\hat{\mathbf{z}}], \quad (3.8)$$

$$M_{rn} = \frac{4B_r}{n\pi\mu_0} \sin\left(\frac{n\pi\delta}{2}\right), \quad (3.9)$$

$$M_{zn} = -\frac{4B_r}{n\pi\mu_0} \cos\left(\frac{n\pi\delta}{2}\right). \quad (3.10)$$

Here,  $\mathbf{M}$  is the magnetization vector,  $M_{rn}$  and  $M_{zn}$  are the radial and axial component of the magnetization for a given harmonic,  $k$  is the wavenumber of the magnet array,  $\delta$  is the fraction of magnet array composed of the radial magnets, and  $B_r$  is the magnetic remnance. The magnetic remnance is the magnetic flux density produced in the absence of a magnetic field. The wavenumber refers to the spatial variation of a sinusoid, and is given by  $2\pi$  divided by the wavelength. In the case of the voice coil, the wavelength is equal to twice the total length of the magnets. The justification of this wavelength can be seen by looking at the spatial variation of the magnetization. The radial magnetization starts out zero at the end of the motor, reaches a maximum at the center of the motor within the radial magnet, and is zero again in the other end. Therefore, the lowest harmonic of the Fourier series is a cosine curve that originates at the motor's center and completes a half wavelength within the motor. Similarly, the axial magnet starts at one value, then flips magnitude at the midpoint. Therefore, the lowest harmonic of the Fourier series is a sine curve that likewise has its origin at the center of the motor and completes a half wavelength within the motor.

With the magnetization thus described by a Fourier series, Poisson's and Laplace's equations can be solved in the magnets and the air gap. The solution is also described by a Fourier series, and has the form given below.

$$\begin{aligned}
\mathbf{H}_{\text{magnet}} &= \sum_{n \text{ odd}} \left[ aI_1(nkr) + bK_1(nkr) + \frac{\pi}{2}M_{rn} (I_1(nkr) - L_1(nkr)) - M_{rn} \right] \\
&\cdot \hat{\mathbf{r}} \cos(nkz) \\
&+ \left[ -aI_1(nkr) + bK_0(nkr) - \frac{\pi}{2}M_{rn} (I_0(nkr) - L_0(nkr)) - M_{rn} \right] \\
&\cdot \hat{\mathbf{z}} \sin(nkz), \tag{3.11}
\end{aligned}$$

$$\begin{aligned}
\mathbf{H}_{\text{air}} &= \sum_{n \text{ odd}} [cI_1(nkr) + dK_1(nkr)] \hat{\mathbf{r}} \cos(nkz) \\
&+ [-cI_0(nkr) + dK_0(nkr)] \hat{\mathbf{z}} \sin(nkz). \tag{3.12}
\end{aligned}$$

In these equations,  $\mathbf{H}$  is the magnetic field vector,  $I_0$  and  $I_1$  are the modified Bessel functions of the first kind,  $K_0$  and  $K_1$  are the modified Bessel functions of the second kind,  $L_0$  and  $L_1$  are the modified Struve functions, and  $a, b, c,$  and  $d$  are arbitrary constants [5]. The field solution matches the form that was expected for this type of geometry, as was described in Section 3.2.1. To solve for the arbitrary constants, the boundary conditions for this geometry are applied. Four are needed, namely that the axial component of the  $\mathbf{H}$  field is continuous across the boundary between the air and magnets, as is the radial component of the  $\mathbf{B}$  field. Additionally, the field is finite when  $r=0$ , and the  $\mathbf{H}$  field inside the iron is zero. This last condition comes from considering the iron to have approximately infinite permeability. Since the  $\mathbf{B}$  field in the iron must remain finite, then by Eq. 3.5 the  $\mathbf{H}$  field must be zero in a material with infinite permeability.

Applying these boundary conditions yields the following values for the coefficients.

$$\begin{aligned} a &= c - \frac{\pi}{2} nkr_m M_{rn} [K_1 (I_0(nkr_m) - L_0(nkr_m)) + K_0 (I_1(nkr_m) - L_1(nkr_m))] \\ &\quad - nkr_m M_{zn} K_1, \end{aligned} \tag{3.13}$$

$$b = 0, \tag{3.14}$$

$$c = d \frac{K_0(nkr_{Fe})}{I_0(nkr_{Fe})}, \tag{3.15}$$

$$\begin{aligned} d &= \frac{\pi}{2} nkr_m M_{rn} [I_0 (I_1(nkr_m) - L_1(nkr_m)) + I_1 (I_0(nkr_m) - L_0(nkr_m))] \\ &\quad - nkr_m M_{zn} I_1, \end{aligned} \tag{3.16}$$

where  $r_m$  is the radius of the magnets and  $r_{Fe}$  is the inner radius of the iron shell in meters.

With the magnetic fields known, it is possible to find the force that the motor can produce, equal to the Lorentz force acting on the coil. The force acting on the coil can be found by integrating the magnetic flux density over the volume occupied by the coil and multiplying by the current density in the coil.

### 3.3 Geometric Optimization

With the solutions to the field equations inside the motor known, the motor's expected force may be expressed in terms of the geometry of the motor. To create a specific motor design, these dimensions can be optimized to produce the maximum force while still fitting within any design constraints. The optimization that led to the design used in this thesis was performed by Bryan Ruddy [8]. The constraints on the optimization were chosen to yield a motor suitable for use in a portable NFI device. The mass of the device was limited to 0.5 kg, and the stroke length was required to be at least 36 mm. Additional constraints were built in to account for the required thickness of the bobbin and the air gap outside of the coil.

To choose the thickness of iron, a value for the maximum allowable magnetic flux density passing through the iron was specified. In the final design, 4.5 T was the largest allowed magnetic flux density in the iron when the actuator was producing 1000 N. Iron saturates at about half this magnetic flux density. This level of magnetic flux density was allowed because, through FEA analysis, it was found that under these conditions, only a fraction of the total iron in the motor was saturated. Furthermore, by allowing a higher level of magnetic flux density in the iron, a larger fraction of the motor's mass could be in the coil and magnets, which led to a larger motor constant. Because some parts of the iron were saturated, however, the assumption made in this model that all the magnetic flux remained in the iron was no longer valid, which caused a decrease in the model's accuracy. The model still held predictive power, however, assuming that the endcaps remained unsaturated. The periodicity of the



motor depends on the  $\mathbf{H}$  field being zero in the endcaps, and thus if the endcaps saturate the field equations used in the model would no longer be accurate.

The optimization was performed in MATLAB. Different values were tried for the magnet radius, the inner iron radius, the outer iron radius, and the fraction of the length occupied by the radial magnets. The force was calculated for these varying dimensions, thus allowing the geometry to be optimized. The final dimensions derived from this optimization are given in Table 3.1.

Table 3.1: The optimized dimensions for the voice coil motor.

Magnet radius	13.4 mm
Inner iron radius	21.8 mm
Outer iron radius	23.0 mm
End cap thickness	2.0 mm
Total magnet length	50.6 mm
Radial magnet length	7.8 mm
Coil length	24.6 mm

In this plan, a bobbin wall thickness of 0.5 mm was allowed, and there was a 0.1 mm air gap between the coil and iron housing. These dimensions formed the basis of the prototyped device.

### 3.4 Finite Element Modeling

The motor's expected performance was verified using Finite Element Analysis (FEA). FEA yielded a more accurate estimate of the motors performance because, unlike the analytical model, the FEA was able to solve the governing equations directly and to account for factors such as the nonlinear saturation of iron. The simulation was not, however, able to account for demagnetization. All FEA simulations were performed using a radially symmetric model in COMSOL Multiphysics [9].

Fig. 3-2 shows an exact solution of the  $\mathbf{B}$  field as found by the FEA when there is no current flowing. As expected, the  $\mathbf{B}$  field forms two loops which combine in the

radial magnet and create a region of high field through the coil.

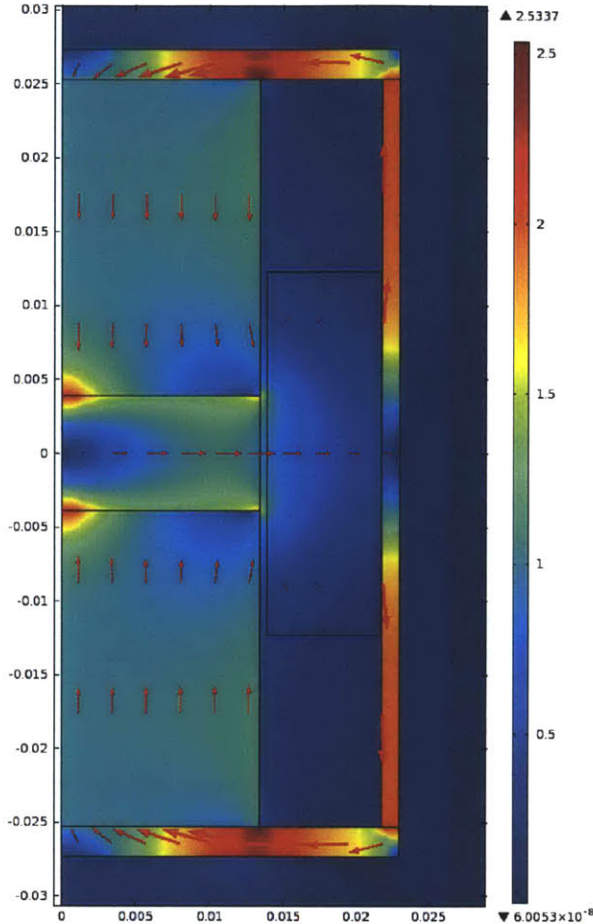


Figure 3-2: The magnetic flux predicted by FEA. The left boundary is the axis of radial symmetry. The colorbar gives the magnetic flux magnitude in Teslas, and the axes the dimensions in meters. The arrows show the direction and magnitude of the magnetic flux, which forms two loops in the motor.

Given in Fig. 3-3 is a plot of the force produced midstroke as a function of current density in the coil. For lower current densities, the plot is linear; in these regions the motor constant is equal to  $11.02 \text{ N}/\sqrt{W}$ . This motor constant was calculated with the assumption that 75% of the volume of the coil was occupied by copper. The motor was designed to be 0.5 kg; with this mass, the mass-scaled motor constant is  $15.50 \text{ N}/\sqrt{W \cdot \text{kg}}$ . At the highest current density shown, motor constant has decreased

slightly because the iron has started to saturate.

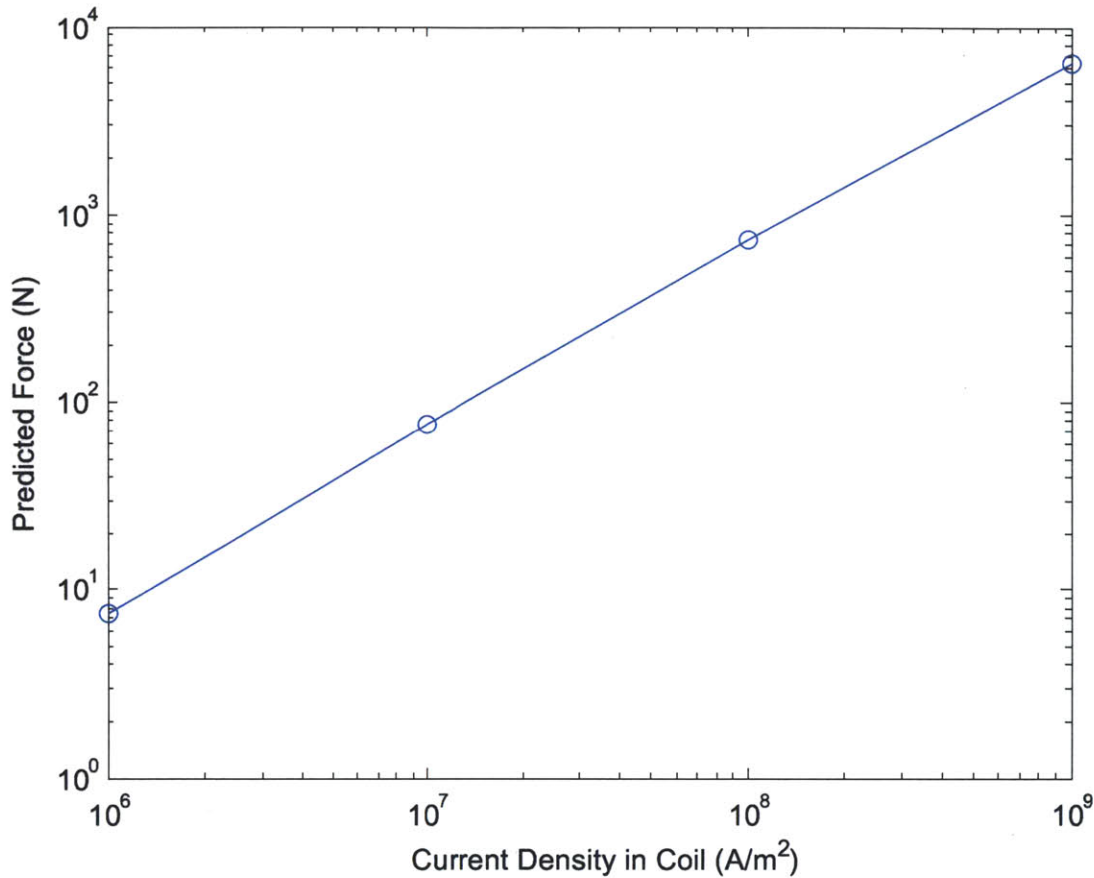


Figure 3-3: The FEA-predicted force when the coil is mid-stroke as a function of current density.

At the ends of the travel, the motor produces less force because the field is not as strong in that region. Fig. 3-4 shows the force as a function of current when the coil has been displaced 9 mm from the center.

The plot includes the force for the current flowing each direction. The two directions are not identical because the coil is attracted to the iron endcap. In one direction, this attraction increases the net force; in the other, it detracts from the net force. At the end of the stroke, the motor constant is  $8.24 \text{ N}/\sqrt{W}$  when the force is directed towards the closer endcap, and  $8.19 \text{ N}/\sqrt{W}$  when the force is directed away.

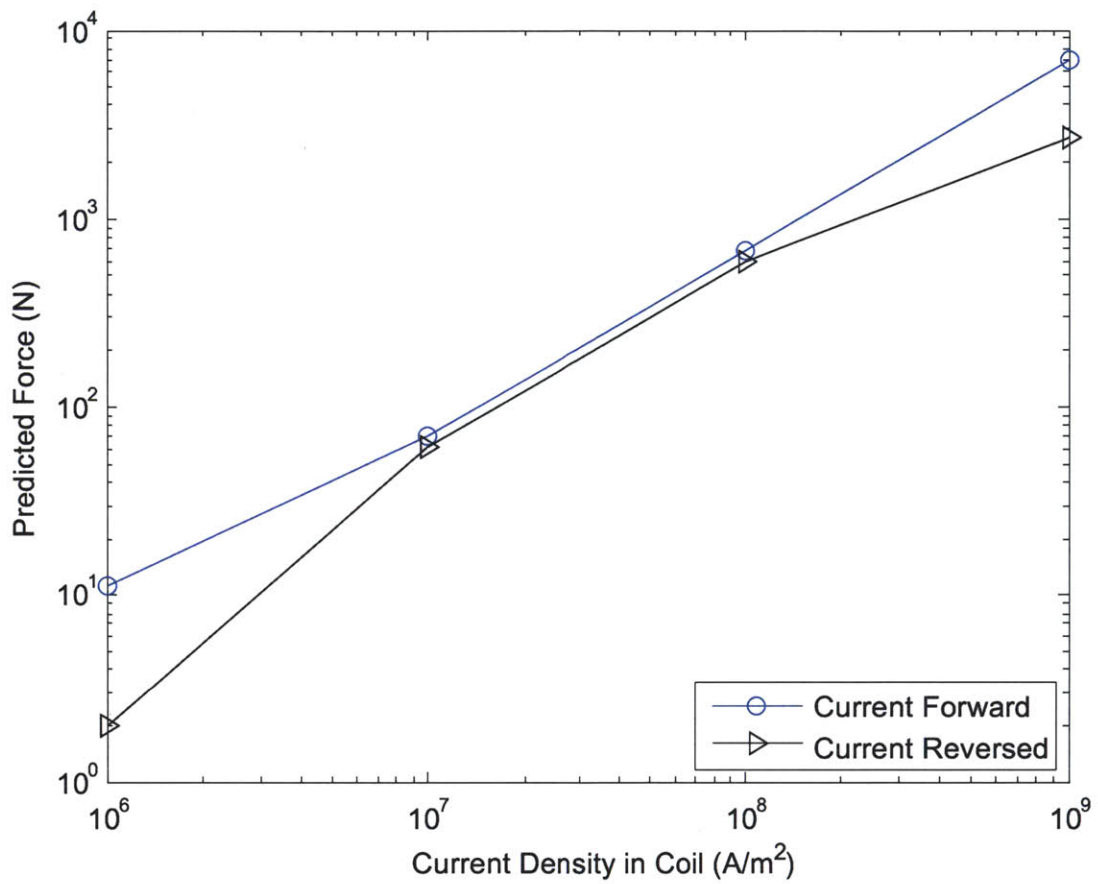


Figure 3-4: The predicted force when the bobbin is displaced by 9 mm from the center, with the current flowing in each direction.

# Chapter 4

## Experiment

To verify the predictions made by the analytical and FEA models, the optimized motor geometry was constructed and tested. This chapter describes the manufacturing of the motor and presents the results of characterization.

### 4.1 Mechanical Design and Manufacturing

The design of the prototyped motor is shown in Fig. 4-1.

On the top and bottom of the motor are the endcaps, which are secured to the outer housing. The housing is transparent in the picture. Inside the housing is the bobbin, which will be wound with copper for the coil. The bobbin rides on the magnet array, which extends from endcap to endcap. Four rods thread into the top of the bobbin and extend out the top of the endcap. These rods will transmit the force from the bobbin to the coil. With this design the motor has a stroke of 15 mm, but the motor has the potential to increase the stroke to 20 mm with minor design adjustments.

The following section details the design choices made and manufacturing techniques used in fabricating the motor prototype.

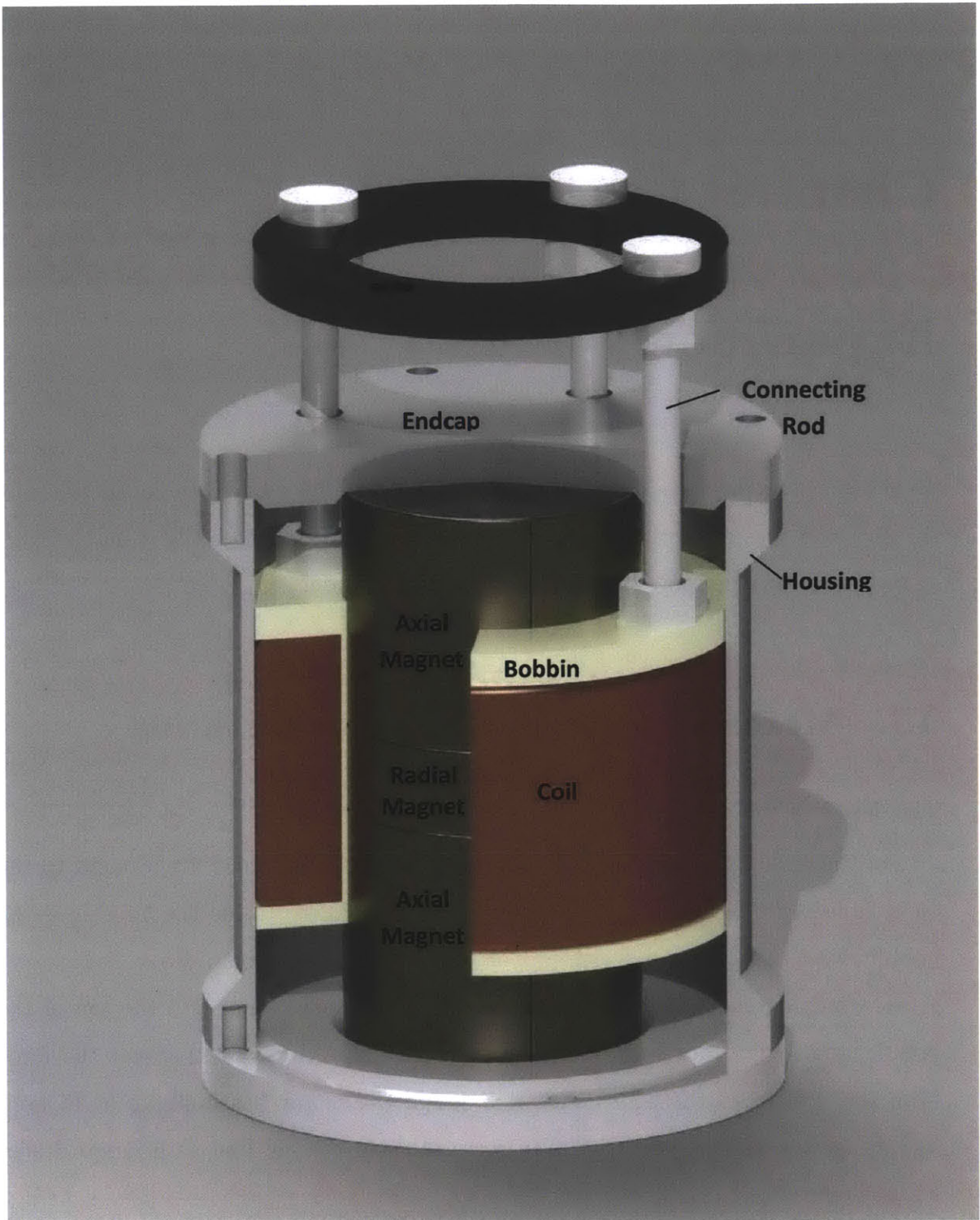


Figure 4-1: The overall design for the motor

### 4.1.1 Endcaps

The endcaps are shown in Fig. 4-2.



Figure 4-2: The endcap. The outermost holes allow the endcap to bolt to the housing, and the four large inner holes allow the connecting rods to pass through. The two additional holes are threaded and used to facilitate disassembly.

Low carbon 1026 steel was chosen for the endcaps. They were designed with a chamfered ring that would make them self-centering within the housing and also allow the magnets to self-center. On one endcap, countersunk holes were created to allow the rods linking the coil and load cell to pass through. On the other endcap, larger throughways were milled to allow the insertion of a tool that would center the magnets during motor assembly. The endcaps were made on a CNC mill using G-code generated by FeatureCAM. The thickness of the endcaps was increased from the 2 mm recommended by the optimization to 4 mm, the thickness required to hold the stock in the mill vise. The throughways for the centering tool were added on a manual mill at a later date.

### 4.1.2 Housing

The motor housing is shown in Fig. 4-3.



Figure 4-3: The motor housing.

Low carbon 1026 was likewise used for the housing. The motor housing was designed to secure the endcaps using four screws per endcap. For this purpose, the thickness of the wall at the top and bottom of the housing was increased to 4 mm, and four tapped M2.5 holes were added on each end. The wall thickness was also increased from the optimization's recommended 1.2 mm to 2.6 mm in order to make the piece less fragile. This modification was done by increasing the outer radius to 24.4 mm and leaving the inner radius at the prescribed 21.8 mm.

Several attempts were made to manufacture the housing on a CNC lathe, using an expanding collet to fixture the stock. A variety of user and machine errors, however, showed that a manual machining process would be more expedient in the short term. Future iterations, however, could be manufactured using a CNC lathe. The turning and boring here were done on a manual lathe and the holes on a manual mill. The resulting part was slightly out specifications: the manufactured inner radius was 21.99 mm, 0.19 mm larger than was called for.

### 4.1.3 Bobbin

The bobbin and coil are shown in Fig. 4-4.



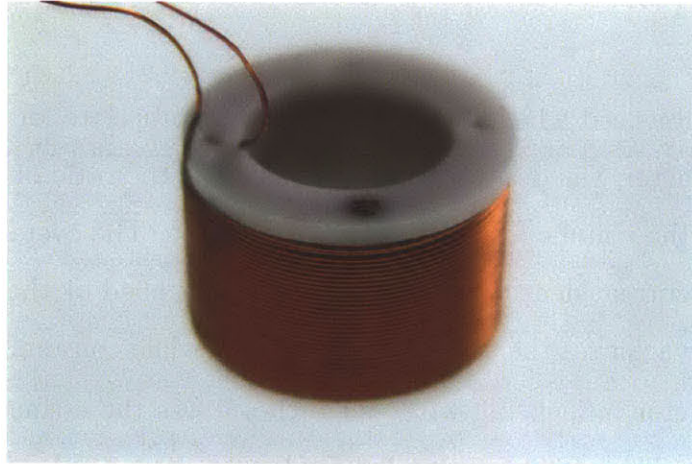


Figure 4-4: The bobbin and coil.

Ultem was initially chosen as the material for the bobbin. A performance plastic, the material was both light and resistant to high temperatures. The material, however, was ultimately switched to Delrin [10]. Acetal Delrin easily accepted the small wall thickness called for in the bobbin, and with a deflection temperature of  $98^{\circ}\text{C}$  at 1.8 MPa, the material should be able to withstand the heat of the operating coil [11]. If temperatures inside the motor approached those temperatures, the magnets would be in danger of demagnetization, showing that the Delrin should be sufficient.

The bobbin was designed with a wall thickness of 0.5 mm. The inner diameter was made to the exact diameter of the magnets, 26.8 mm, in order to use the magnets as a linear bearing. A gap of  $100\ \mu\text{m}$  was left between the outer surface of the bobbin and the inner surface of the housing. The bottom ridge of the bobbin was chosen to be 2 mm thick. The top ridge was made 3 mm thick; the increased thickness allowed for threaded holes to be placed in the top. Rods threading into these holes linked the coil to the load cell. Two 1 mm holes drilled on the top ridge provided entrance and exit points for the wire. The bobbin was manufactured using a Mazak Turning Center [12].

#### 4.1.4 Coil

Several factors influenced which gauge of wire was appropriate for winding the coil. First, a high fill factor was desirable. The fill factor is the ratio of the volume filled the conductor to the volume available to the conductor. The overall current density for the coil is the current density in the conductor multiplied by the fill factor. Thus, a higher fill factor achieves the same current density while consuming less power.

The second factor influencing wire gauge choice was the estimated resistance of the resulting coil. The motor is intended for high current applications, and to test the motor at the highest power possible, the coil's resistance should be optimized to draw the most power possible from the available power amplifiers. In the Bioinstrumentation Laboratory, the two available power amplifiers were able to provide 30 A at 300 V and 100 A at 100 V. Thus, to be able to the maximum power from each, the coil should have a resistance of 10  $\Omega$  and 1  $\Omega$  respectively. Two more factors influenced the choice of wire: the wire should wrap around the bobbin to form an even number layers, and the wire should be an even AWG value. The first condition allows the wire to enter and exit on the same side, and the second limits the choices to the gauges which are readily available.

Analysis showed that 22 gauge wire was the best option. This wire was expected to provide an adequate fill factor (57%) and a resistance that was between the optimal values for the two amplifiers. The wire would wrap an even number of times (10), and it was of an even gauge.

When the coil was wound by hand, it was found that 12 layers were able to fit onto the bobbin, instead of the expected 10. These extra layers increased the fill factor to 74.5%, calculated based on the mass of the bobbin. The resistance of the resulting coil was 2.59  $\Omega$ , and the mass was 0.1430 kg. The ends of the wires were pressed into grooves that had been made in one of the rods that connected the bobbin to the load cell. The wires exited the groove on the exterior of the motor and were connected to a power supply.

### 4.1.5 Magnets

The magnets are shown in Fig. 4-5.

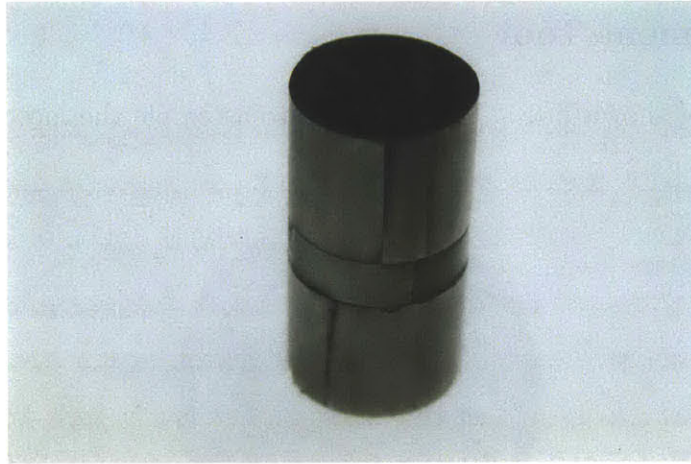


Figure 4-5: The magnet assembly, composed of a radial magnet sandwiched between two opposing axial magnets.

The magnets were made from NdFeB stock supplied by Vacuumschmelze [?] that had a magnetic remnance of 1.344 T. They were cut from the stock using a Wire Electric Discharge Machine (EDM).

To create a radial magnet, four quarter circles of the appropriate height were cut out. With each one magnetized in the radially outward direction, their combined behavior simulated that of a radial magnet. The axial magnets could have been cut from a single piece, but the 26.8 mm diameter of the magnets was too large to fit into the magnetizer, which accepted a maximum of 25 mm. To be able to fit in the magnetizer, the axial magnets were assembled from components, each of which comprised one third of a circle.

The magnets were magnetized in a magnetization machine built by Bryan Ruddy. The device used six lead acid batteries to supply high current to a coil for a period of 50 ms. The magnets were placed at the center of the coil. As the current flowed through the coil, the magnets were exposed to a high magnetic field and instantly magnetized.

After magnetization, the components of the magnets were then assembled into one structure, bound by Loctite 1C-LV Hysol Epoxy Adhesive [?].

#### 4.1.6 Alignment Tool

An alignment tool shown in Fig.4-6, was used to assemble the motor.



Figure 4-6: The alignment tool is shown inserted through the bottom endcap.

The alignment tool was made on the Wire EDM and the Manual Mill. Its outer diameter fit snugly against the motor housing, and its inner diameter securely gripped the magnets. During assembly, the alignment tool was inserted through the holes in the bottom endcap so that its legs protruded into the motor housing. The magnets were then fed into the alignment tool, which constrained them to stay in the exact center of the housing. The magnets were attracted to the bottom endcap, which allowed them to remain in alignment when the tool was removed.

## 4.2 Testing and Characterization

This section details the initial tests used to characterize the performance of the motor. Relatively small levels of current were applied, supplied through a desktop power

supply.

#### 4.2.1 Experimental Setup

The assembled motor was characterized by measuring the force produced when different levels of current were applied. The setup for applying current and measuring force is showing in Fig. 4-7.

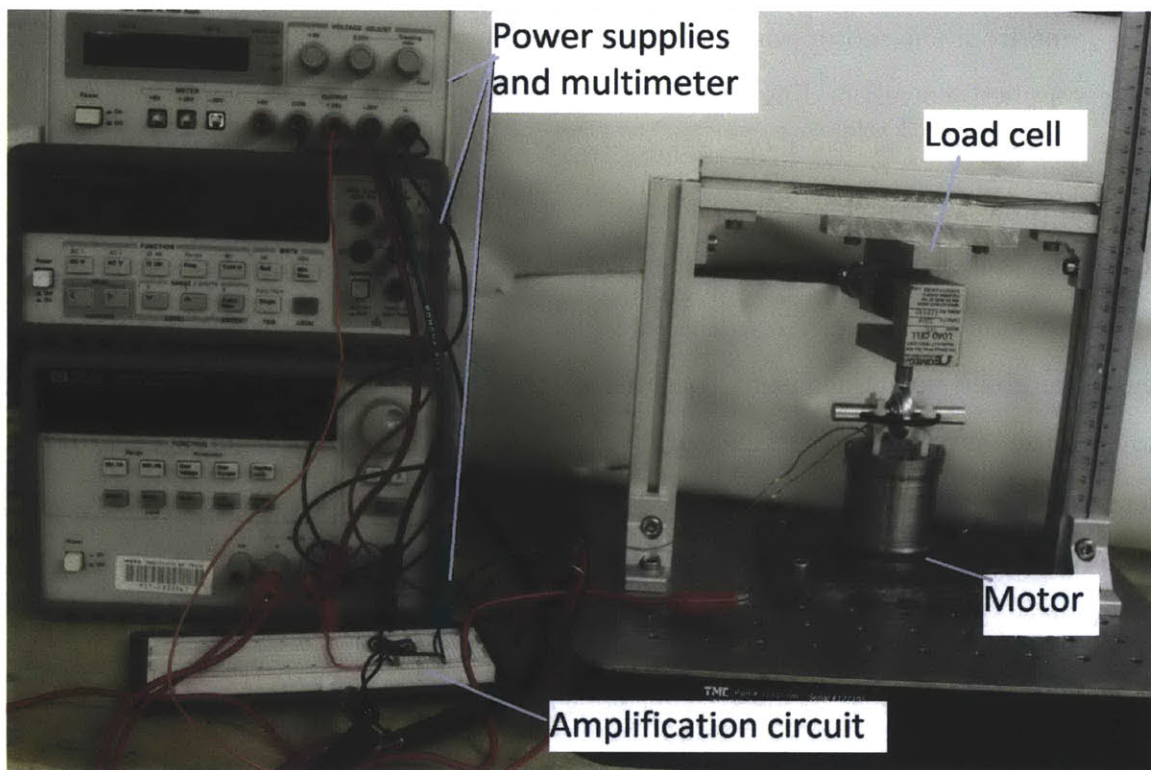


Figure 4-7: The testing setup.

The motor was bolted to a benchtop optical table, and an Omega S Beam Load Cell was suspended above the motor using an MK frame. The load cell had a maximum load of 900 N. A ball joint threaded into the load cell and coupled to the connecting rods on the motor, thus linking the load cell and the coil. Power was supplied to the motor through a HP E3632A DC power supply, which was able to produce 7 A at 15 V. A second power supply, an Agilent E3630A, provided 10 V

to the load cell and  $\pm 10$  V to the amplification circuit. The amplification circuit used an Analog Devices AMP02 instrumentation amplifier with a gain of 334 to feed the signal from the load cell into an Agilent 34401A Digital Multimeter. Calibration of the load cell yielded a calibration constant of 78.1 N/V.

## 4.2.2 Experimental Results

The force from the motor was measured when currents of 1.000, 3.000, and 5.000 A were supplied, corresponding to an overall current density in the coil of  $2.295 \cdot 10^6$ ,  $6.885 \cdot 10^6$ , and  $1.148 \cdot 10^7$  A/m<sup>2</sup>. These tests were performed with the current flowing in both directions, placing the load cell both in tension and compression. The force was measured at six positions in the stroke: the midpoint, and displacements of  $\pm 3$  mm,  $\pm 6$  mm, and  $-9$  mm from the midpoint. The displacement of  $+9$  mm from the midpoint could not be measured because a guard kept the coil away from the endcap so that the entering and exiting wire would not be pinched. Each measurement was repeated four times. The force as a function of axial displacement for these currents is shown in Fig.4-8

As expected, the force is maximum in the middle of the stroke and decreases with distance away from the center. The shape of the force versus distance curve can be explained by recalling that the radial field varies sinusoidally in the axial direction. The cosine originates at the midpoint and goes to zero at the endcaps, which are each a quarter wavelength from the center. The coil has a finite length, so at any point in the stroke it intersects some fraction of the radial field. Since the force is proportional to the integral of the radial field along the length of the coil, displacements of the coil cause the force to vary as the window of integration captures different portions of the cosine curve.

The measured forces in tension and compression are of almost equal magnitude. The measurements taken in compression were taken after the measurements in tension; the smaller uncertainty in this data reflects the operator's increased competence

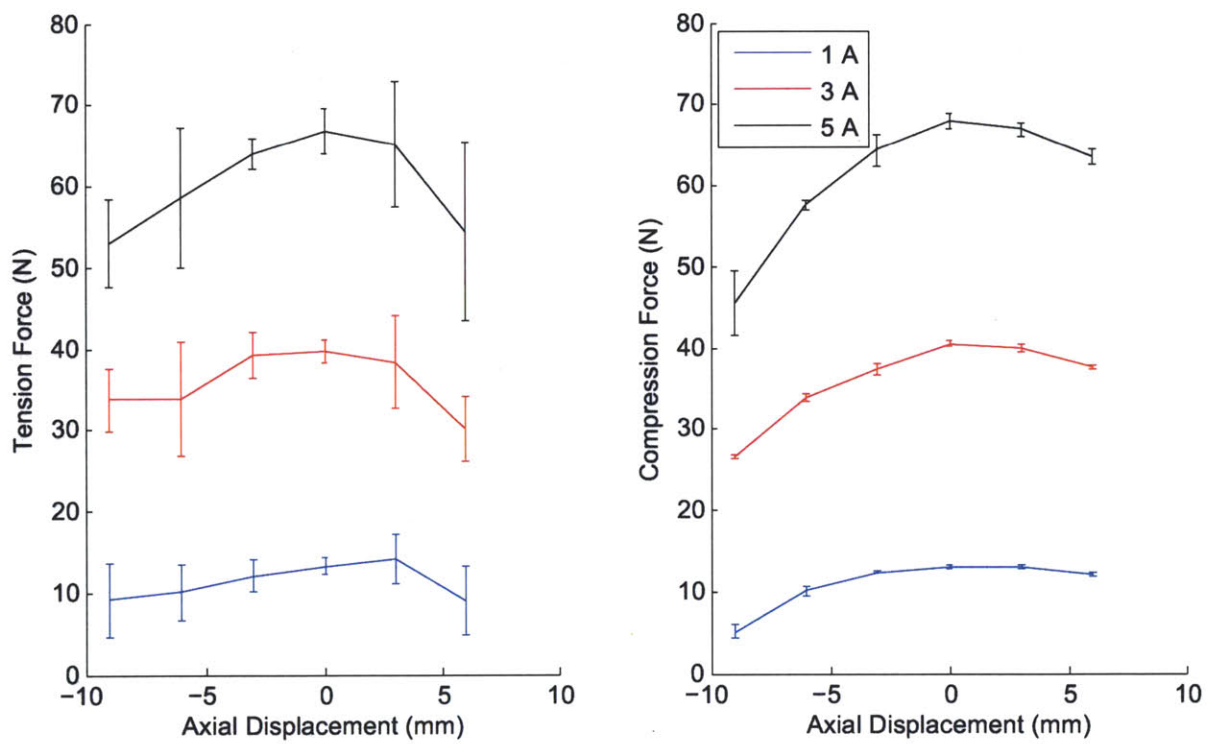


Figure 4-8: The measured force as a function of the location in the stroke. The error bars shown are the 95% confidence intervals for each value.

in taking consistent measurements.

The motor constant for this motor is  $8.42 \text{ N}/\sqrt{\text{W}}$  at the center, the average of measured value of  $8.31 \text{ N}/\sqrt{\text{W}}$  when the load cell was put in tension, and  $8.53 \text{ N}/\sqrt{\text{W}}$  when the load cell was put in compression. This motor constant is about 25% less than the value expected value of  $11.02 \text{ N}/\sqrt{\text{W}}$ , which was calculated using the FEA model. The measurements taken at -9 mm yielded a motor constant of  $6.80 \text{ N}/\sqrt{\text{W}}$  in tension and  $6.27 \text{ N}/\sqrt{\text{W}}$  in compression. At this location, the FEA model predicted  $8.24 \text{ N}/\sqrt{\text{W}}$  in tension, and  $8.19 \text{ N}/\sqrt{\text{W}}$  in compression, thus, the measured values are about 20% less than the expected ones. Fig. 4-9 shows the force measured at the center of the stroke as a function current; also shown are the forces expected at these currents based on the FEA simulations.

On average, the measured force is 25% lower than the FEA-predicted value, matching the decrease seen in the motor constant. To diagnose the cause of the force reduction, the magnetic field outside the motor and in the gap was measured with a FW Bell Gauss/Teslameter 5080 [15]. The results of this examination showed that the actual field agreed reasonably well with the predicted fields. The field was measured in the gap by removing the coil from the motor and inserting the Teslameter probe through the hole in the endcap usually occupied by the connecting rods. Inside the motor, a maximum radial magnetic flux density of 0.968 T was measured close to the radial magnet. In the FEA simulation, the maximum radial magnetic flux density was 1.23 T. The region with this flux density was very small, however, and was located next to the boundary between the radial and axial magnets. Along most of the radial magnet, the flux density was about 1 T. It is possible that the Teslameter, being fed from a hole in the endcap, was unable to effectively measure the small region with the highest field, in which case the measured value agrees fairly well with the FEA prediction. Outside the motor shell, a maximum radial field of 0.015 T was measured, compared to about 0.08 T predicted by the FEA simulation. The extra thickness of the endcaps could account for more of the field being contained in the



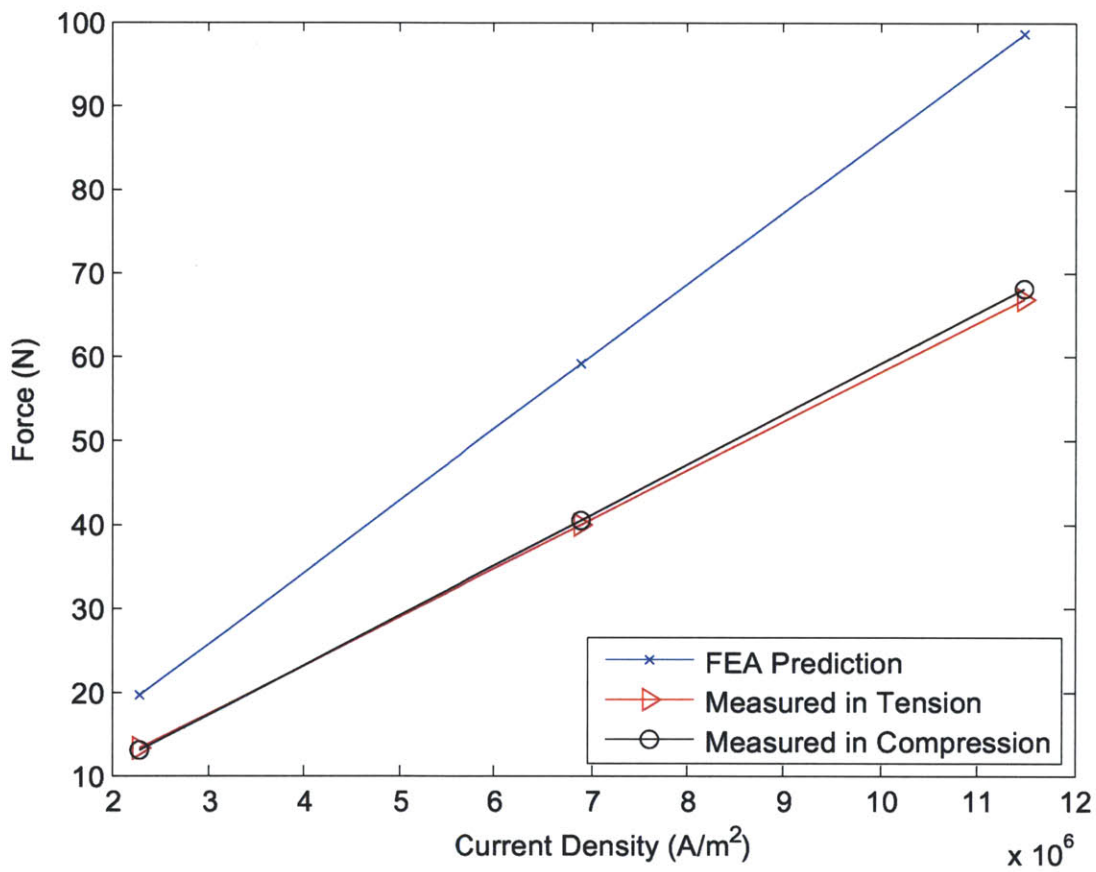


Figure 4-9: A comparison of the measured force to the FEA-predicted values when the coil is midstroke.

magnetic circuit.

# Chapter 5

## Conclusion

An optimized motor has been developed that shows promise as a high power, high force actuator. This motor uses two opposing magnets to increase the magnetic flux through the coil. Initial tests demonstrate that the motor is a more powerful actuator than the model currently in use in NFI, with a motor constant of  $8.43 \text{ N}/\sqrt{\text{W}}$ , compared to  $3.21 \text{ N}/\sqrt{\text{W}}$  for the current model. The maximum magnetic flux density measured in the gap was  $0.968 \text{ T}$ , compared to  $0.6 \text{ T}$  for the prior model. At  $0.5812 \text{ kg}$ , the constructed motor remains lightweight enough for portable applications. Future improvements, such as decreasing the thickness of the endcaps, would enable the motor to match the current model's mass of about  $0.5 \text{ kg}$ , with no expected decline in performance. Currently, the mass-scaled motor constant for this motor is  $11.07 \text{ N}/\sqrt{\text{W} \cdot \text{kg}}$ , compared to  $4.54 \text{ N}/\sqrt{\text{W} \cdot \text{kg}}$  for the prior motor model. Again, this parameter will improve when the mass of the motor decreases in future iterations.

The constructed motor produces about 25% less force than was predicted by FEA. Measurements show that the field in the constructed motor is slightly less than the FEA predicted, and thus further work is needed to definitively determine the cause of the motor's decreased performance. Future work would also include testing at the higher current densities that would be used in an NFI device. Based on the initial tests, this device shows promise as a way to deliver more viscous fluids via NFI.



# Bibliography

- [1] Hemond, B.D., Taberner, A.J., Hogan, N.C., Crane, B. and Hunter, I.W. “Development and Performance of a Controllable Autoloading Needle-free Jet Injector.” *Journal of Medical Devices*. Vol. 5, 2011.
- [2] Taberner, A.J., Hogan, N.C. and Hunter, I.W. “Needle-free Jet Injection Using Real-time Controlled Linear Lorentz-force Actuators.” *Medical Engineering & Physics*(2012), doi:10.1016/j.medengphy.2011.12.010.
- [3] Yadev, S., Shire, S.J. and Kalonia, D.S. “Viscosity Behavior of High-concentration Monoclonal Antibody Solutions: Correlation with Interaction Parameter and Electroviscous Effects.” *Journal of Pharmaceutical Sciences*. Vol. 101(3), 2012.
- [4] Einmahl, S., Capancioni, S., Schwach-Abdellaoui, K., Moeller, M., Behar-Cohen, F. and Gurny, R. “Therapeutic Applications of Viscous and Injectable Poly(ortho esters).” *Advanced Drug Delivery Reviews*. Vol. 53, 2001.
- [5] Ruddy, B.P. and Hunter, I. W. “Design and Optimization Strategies for Muscle-like Direct-drive Linear Permanent-magnet Motors.” *International Journal of Robotics Research*. Vol. 30(7), 2011.
- [6] Ball, N.B. An Optimized Linear Lorentz-force Actuator for Biorobotics and Needle-free Injection. Thesis for Master of Science, MIT, 2007.

- [7] Taberner, A.J., Ball, N.B., Hogan, N.C. and Hunter, I.W. "A Portable Needle-free Jet Injector Based on a Custom High Power-density Voice-coil Actuator." *Proceedings of the 28th IEEE EMBS Annual International Conference*. New York, 30 Aug 2006.
- [8] Ruddy, B.P. Electromagnetic Muscle Actuators: High Force Density Direct-drive Linear Permanent Magnet Motors. Thesis for Doctor of Philosophy, MIT, 2012.
- [9] COMSOL Multiphysics, COMSOL, Inc. <http://www.comsol.com/>
- [10] DuPont Delrin acetal resin. [http://www2.dupont.com/Plastics/en\\_US/Products/Delrin/Delrin.html](http://www2.dupont.com/Plastics/en_US/Products/Delrin/Delrin.html)
- [11] Matweb. DuPont Performance Polymers Delrin®| 150E BK602 Acetal. <http://matweb.com/>. Accessed May 2012.
- [12] Mazak Corporation. <http://www.mazakusa.com/>
- [13] Vacuumschmelze. <http://www.vacuumschmelze.de/>
- [14] Loctite) Loctite 1C-LV Hysol Epoxy Adhesive, Henkel Corporation. <http://www.loctite.com/>
- [15] Meggitt Equipment Group. <http://fwbell.com/>